# Voiding mechanisms in deformed polyamide 6 observed at the nanometric scale

Nathan Selles, Peter Cloetens, Henry Proudhon, Thilo F. Morgeneyer, Olga Klinkova, Nicolas Saintier, Lucien Laiarinandrasana

HAL Id: hal-01549074

https://minesparis-psl.hal.science/hal-01549074

Submitted on 30 Sep 2022

# Voiding Mechanisms in Deformed Polyamide 6 Observed at the Nanometric Scale

Nathan Selles,[*,†] Peter Cloetens,[‡] Henry Proudhon,[†] Thilo F. Morgeneyer,[†] Olga Klinkova,[†,§] Nicolas Saintier,[∥] and Lucien Laiarinandrasana[†]

[†]Centre des Matériaux, CNRS UMR7633, PSL-Research University, MINES ParisTech, BP 87, F-91003 Evry, Cedex, France
[‡]European Synchrotron Radiation Facility, BP 220, 38043 Grenoble, Cedex, France
[§]Institut Supérieur de Mécanique de Paris, QUARTZ (EA 7393), 3 rue Fernand Hainaut, 93407 Saint-Ouen, France
[∥]I2M-DuMAS, CNRS UMR5295, Arts et Métiers ParisTech, Esplanade des Arts et Métiers, 33405 Talence, France

**ABSTRACT:** Micromechanisms of deformation and cavitation within the spherulitic microstructure of a polyamide 6 (PA6) material have been observed with a true spatial resolution of 50 nm by magnified synchrotron radiation holotomography. Smooth round bars in PA6 were submitted to interrupted monotonic tensile tests. Before the engineering peak stress, only pre-existing nanometric voids were identified. At the peak stress, void growth and coalescence have been observed in the neck and 2 mm apart from the neck along the revolution axis. Two kinds of cavity arrangements have also been identified, studied quantitatively, and attributed to specific regions of the deformed spherulites. Voiding appeared in the equatorial plane of the spherulites as diffuse annular voided zones, and polar fans were characteristically penny-shaped voids stacked in columns parallel to the loading axis in the spherulite poles. A cylindrical volume located at the center of these spherulites remained intact (no voids).

## 1. INTRODUCTION

Mechanical behavior and the durability of semicrystalline polymers have to be assessed with accuracy because of the increasing use of these materials in engineering structures. Macroscopic behavior is mainly characterized by the evolution of global variables such as engineering stress and strain. The present paper deals with another approach: the assessment, at micrometric and nanometric scales, of the micromechanisms of deformation and cavitation in a smooth specimen made of thermoplastic polyamide 6 (PA6) deformed under steady strain rate. Microstructural evolution of semicrystalline polymers as bulk materials, such as polyamide 6,[1] poly(vinylidene fluoride),[2,3] and poly(methyl methacrylate),[4] or as matrix for short fiber reinforced composite[5] during monotonic tensile loading on smooth specimens has been reported widely in the literature. Necking and whitening appear on smooth specimens at the peak stress of the engineering stress−strain curve and have been related to voiding mechanisms that occurs at the microscopic scale within the material. A variety of observation techniques have been used to identify and understand these voiding mechanisms. For instance, scanning electron microscopy (SEM) inspections have been performed by Boisot et al.[6] to study the cavitation in a polyamide 11. However, this technique is destructive: samples have to be cut, and surface metallization could be necessary (Au or Au−Pd like). Incoherent polarized steady light transport[7,8] and X-ray scattering[9] have been used on semicrystalline polymers to assess cavitation features at the nanometric scale on 2D slices of

matter and only provide average information within the volume constituted of a stack of these studied slices. This averaging procedure may suppress gradients of the inspected variables, and choosing the size of the volume of interest can be tricky. 3D X-ray inspection techniques and especially synchrotron radiation computed tomography or laminography (SRCT and SRCL) can be considered as nondestructive and do not require any tedious preparation of the samples. SRCT has been used to study notched round bars in PA6 deformed ex situ under steady strain rate[10] or under steady load.[11,12] Microstructure of less dense matter, assumed to be voids, has been visualized in 3D with resolutions up to 0.7 $\mu$m, and spatial gradients of void volume fraction and void morphology have been studied. Indeed, the tomography and laminography techniques allow through thickness inspections of the samples.[13] Notched round bars in PA11 deformed in situ have also been observed by SRCT[14] in order to compare ex situ and in situ tests in terms of voiding phenomena. Laiarinandrasana et al.[1] studied an initially smooth round specimen in PA6 deformed under steady strain rate up to the end of the stress softening, when the neck was well extended. Then, they performed SRCT inspections in the neck of the deformed specimen, and they identified cylindrical cavities, stretched in the loading direction and organized in columns called polar fans.[15,16] The resolution of these
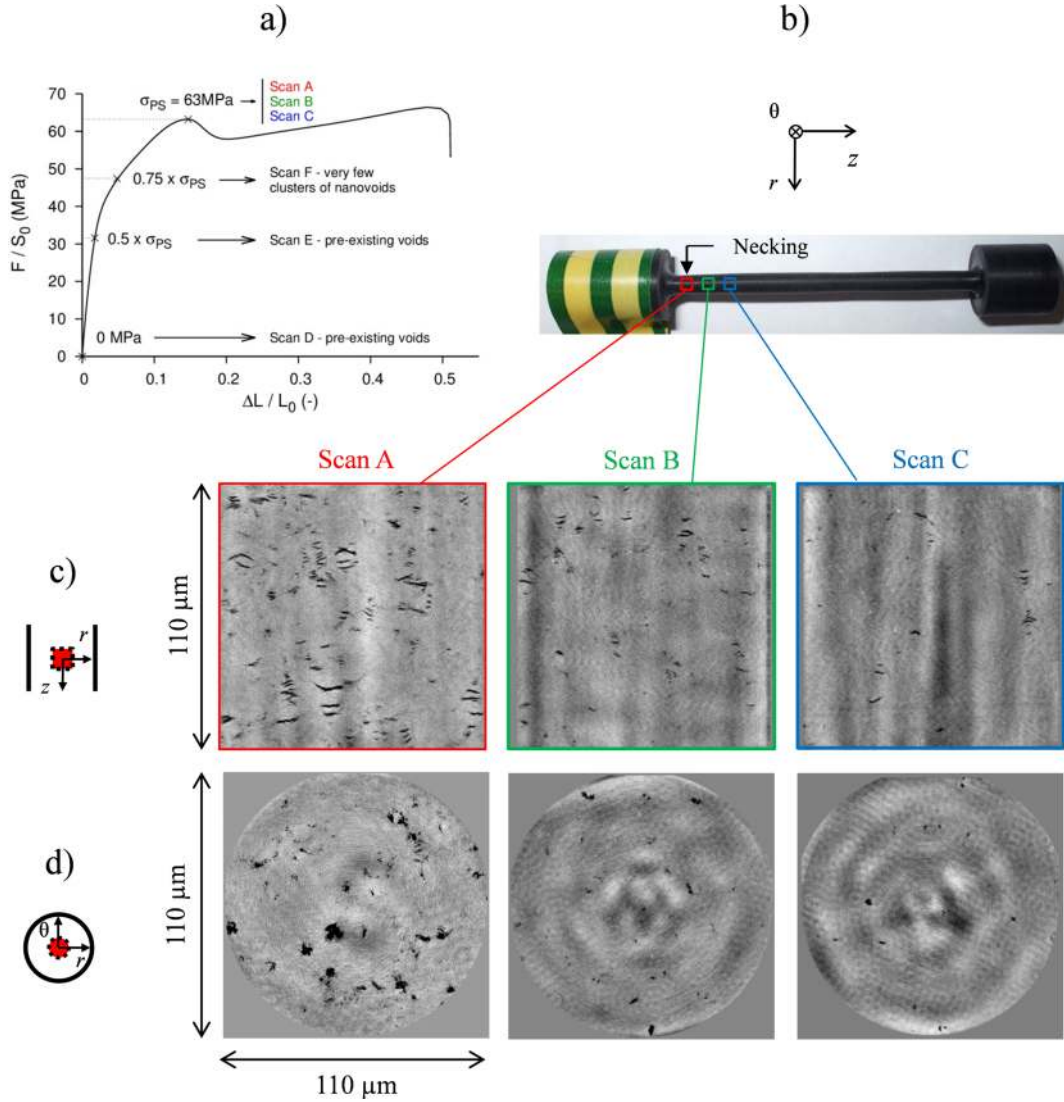
**Figure 1.** (a) Engineering stress−strain curve. (b) Location of the volumes of interest (scans A−C) in the PA6 round bar deformed up to the peak stress. (c) Longitudinal tomographic views ($rz$ plane). (d) Circumferential tomographic views ($r\theta$ plane).

tomographic images was close to a micrometer and was not sufficient to assess with accuracy the early stages of voiding mechanisms, especially the void growth mechanisms before the peak stress. The purpose of the present work is to complete these studies employing the magnified holotomography technique, as used by Morgeneyer et al.[17] to study, at the nanometric scale, the spatial distribution of voids in the neck of a HDPE specimen deformed under steady strain rate. Thus, monotonic tensile tests on initially smooth round bars have been carried out and interrupted at the onset of the necking phenomenon that is at the peak of engineering stress and before. The cavitation features have been assessed with a resolution of 50 nm, more than 10 times higher than the best resolutions reached in the previous studies. To the author's best knowledge, it is the first time that the early stages of cavitation and the coalescence phenomenon of nanometric voids have been observed in 3D in a polyamide 6.

These observations first allow a qualitative discussion about void growth and arrangement within a deformed spherulite. The cavitation features are displayed through 2D tomographic slices (longitudinal or circumferential views) and 3D views and are associated with specific regions of the deformed spherulites.

Then, void arrangements encountered in a specimen deformed up to the peak stress are studied quantitatively in a statistical way. Their dimensions are recorded, and the results from a tomographic volume located in the neck and another volume located 2 mm from the neck along the revolution axis are compared.

## 2. MATERIALS AND METHODS

**2.1. Material Description.** The material under study is a thermoplastic polyamide 6 (PA6). Samples were machined from a 610 mm × 1230 mm flow molded plate with 10 mm thickness provided by Angst & Pfister. This process ensured a good homogeneity of the microstructure within the plate. Samples were machined from the center of this plate, which is the part unaffected by thermal gradient. Indeed, a skin of 60 $\mu$m thickness where the mean size of the spherulites is smaller has been identified at the surface of the plate.[18] Thermoplastic PA6 material is known to be hydrophilic: specimens were preconditioned in the testing room at 20 °C and at relative humidity (RH) of 50% until they reached the stabilized water uptake of 1.8%. The properties of this semicrystalline polymer have been published elsewhere,[19] the main ones being recalled here. The glass transition temperature $T_g$ = 4 °C, the melting point $T_f$ = 219 °C, and the crystallinity index $\chi$ = 43% have been determined using the

modulated differential scanning calorimetry (MDSC) technique. The spherulitic microstructure of the PA6 has been studied by scanning electron microscopy (SEM) inspections of chemically etched surfaces.[18] The identified spherulites have a spherical shape and a mean diameter of about 5 $\mu$m. To reveal the presence of pre-existing voids within the undeformed material, samples broken in liquid nitrogen (cryo-fractography technique) have been examined by SEM. Spherical voids with a mean diameter around 0.1 $\mu$m have been observed on these fractured surfaces. The initial void volume fraction ($V_f$) has been estimated at about 1%.

**2.2. Samples Preparation.** A tensile test up to failure was performed on a smooth round bar at room temperature (20 °C) and at an engineering strain rate of 0.01 s$^{-1}$ using an electromechanical testing machine provided with a load cell. The initial gauge section diameter was 3 mm, and the initial gauge length was 40 mm. The loading curve, that is, the engineering stress $F/S_0$ (where $F$ is the load and $S_0$ is the initial cross section) plotted against the engineering strain $\Delta L/L_0$ (where $\Delta L$ is the crosshead displacement and $L_0$ is the initial gauge length), is given in Figure 1a. Thereafter, other monotonic tensile tests have been performed and interrupted at different values of engineering stress: (i) at the peak stress (corresponding to $\sigma_{PS} = F/S_0$ = 63 MPa); (ii) at 75% of the peak stress value (corresponding to $\sigma = F/S_0$ = 47.25 MPa); (iii) at 50% of the peak stress value (corresponding to $\sigma = F/S_0$ = 31.5 MPa). Then the samples have been unloaded. The sample deformed up to the peak stress is represented in the unloaded state in Figure 1b. The nascent neck is located near the shoulder of the sample's head, presumably due to heterogeneous deformation in this region.

**2.3. Holotomography Technique.** The novelty here has been the use of the magnified holotomography technique at the ESRF beamline ID22NI,[20] that is, tomography with a coherent and divergent X-ray beam. A holographic reconstruction procedure combines images taken at different distances from the specimen. It results in quantitative phase mapping and, through association with three-dimensional reconstruction, in holotomography, the complete three-dimensional mapping of the density in a sample. This technique provides higher resolution and has been presented by Morgeneyer et al.[17] in a paper dedicated to the study of void morphologies in a deformed HDPE. Tomographic setups used in the present study are similar to the ones used by Morgeneyer et al.[17] 2000 projections were acquired over 360°, the exposure time was 0.25 s per frame, and the isotropic reconstructed voxel size was 50 nm. More details can be found in Bleuet et al.[21]

The reconstructed 3D volumes are cylindrical (height 110 $\mu$m, diameter 110 $\mu$m), and three locations of interest have been observed within the sample deformed up to the peak stress (Figure 1b). These inspected volumes have been centered on the revolution axis ($z$-axis) of the deformed round bar. Scan A has been located in the nascent neck, where the specimen section diameter was the lowest. Scans B and C have been shifted along the revolution axis of the sample respectively by 2 and 4 mm (Table 1). In the longitudinal view ($rz$

**Table 1. Axial Evolution of Void Volume Fraction ($V_f$) along the Revolution Axis of the Specimen**

|  | scan A | scan B | scan C |
| --- | --- | --- | --- |
| axial distance from the neck (mm) | 0 | 2 | 4 |
| void volume fraction (%) | 4.1 | 1.4 | 0.6 |

plane), tomographic slices are rectangular (Figure 1c), and in the horizontal or circumferential view ($r\theta$ plane), tomographic slices are circular (Figure 1d).

The other samples, deformed up to 50% and 75% of the value of the peak stress, together with an undeformed sample have been inspected using the holotomography technique. Scans D, E, and F refer respectively to the undeformed specimen, to the specimen deformed up to 50% of $\sigma_{PS}$, and to the specimen deformed up to 75% of $\sigma_{PS}$. Circumferential views of these scans are represented in Figure 2.

## 3. RESULTS

**3.1. Axial Evolution of Porosity.** Figure 1 displays 2D reconstructed slices in scans A, B, and C. Voids are well-defined and in black. PA6 bulk is in gray. Diffuse black and white stains and concentric rings can be observed, especially in scan C, and are considered as reconstruction artifacts. The number of voids in each slice and their sizes decrease from scan A to scan C. Indeed, the necking phenomenon on smooth specimens is a localization phenomenon due to micromechanisms of deformation and cavitation within the material: necking initiates where the void volume fraction is maximum. Thus, the voiding state observed in scan A was the most advanced voiding state within the sample. Void volume fraction ($V_f$) is defined as the total volume of voids divided by the whole volume of the tomographic scan. It is obtained by thresholding of the gray level images. Values of $V_f$ for each scan are recalled in Table 1. $V_f$ decreases from scan A to scan C. Such an axial gradient of $V_f$ has also been reported along the revolution axis of notched round bars in PA6 deformed under steady strain rate[10] and steady load[11] at the necking stage.

Starting from the undeformed state and while the macroscopic deformation increased, it would have been interesting to follow porosity at the location of the most advanced voiding state (in the center of the neck at the peak stress for example). However, it is impossible to locate this zone of maximum porosity before the onset of the necking phenomenon on smooth specimens. In order to evaluate the evolution of the cavitation at different development stages, scans D, E, and F (Figure 2) have been centered on the revolution axis ($z$-axis) of the round bars, at an equal distance from the samples' heads. In scans D and E, some nanometric voids can be observed. They correspond to the population of pre-existing voids, responsible for the initial void volume fraction estimated at 1% thanks to SEM inspections. In scan F, the voiding state seems to be more developed since some of these nanometric voids had started to be organized as clusters. Finally, no large voiding phenomena have been identified at the inspected locations before the peak stress. That is why micromechanisms of cavitation along the revolution axis at a given macroscopic deformation (at the peak stress) have been studied in this paper. Scans B and C depict voiding states similar to the most advanced voiding states encountered at a given load before the peak stress. Along the revolution axis of the specimen the whole story of deformation and cavitation has been captured.

**3.2. Void Growth and Coalescence at the Nanometric Scale.** Three populations of voids, characteristic of void growth mechanisms, have been observed in scan A and are represented in a longitudinal tomographic view ($rz$ plane) displayed in Figure 3. Nanometric voids organized in a cluster (see red box in Figure 3) have been identified and have spherical shapes with diameters between 0.1 and 0.5 $\mu$m. They could be related to the population of pre-existing voids observed by SEM in the undeformed state and shown in Figure 2. The improved resolution reached here, thanks to the magnified holotomography technique, has allowed the identification of this population in an unprecedented way. These nanovoids then coalesce (blue box), leading to a cluster of voids with an overall shape similar to that of a flat cylinder. This cylinder can be seen as a volume of less dense matter than the matrix, considered as an individual cavity in observations with a resolution of 0.7 $\mu$m.[10] Finally, this coalescence phenomenon results in the creation of micrometric voids by rupture of intervoid fibrils,
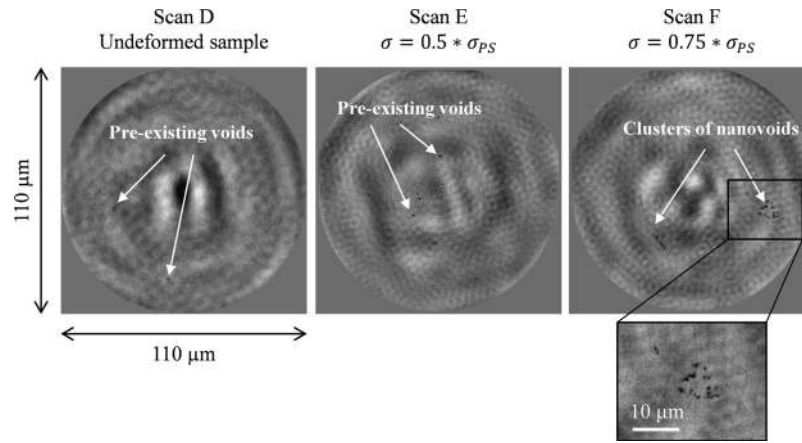
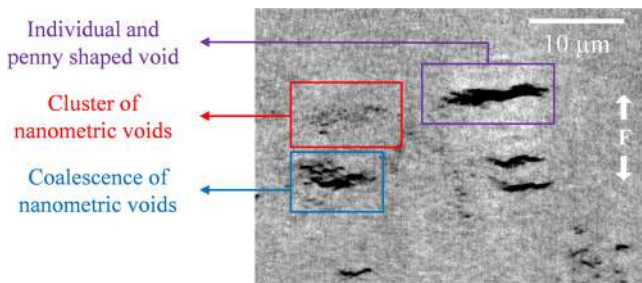**Figure 2.** Circumferential tomographic views ($r\theta$ plane) of scans D−F.



**Figure 3.** Longitudinal view ($rz$ plane) of the three populations of voids in scan A.



**Figure 4.** Diagram of a longitudinal section ($rz$ plane) of a deformed spherulite defining the equatorial, polar, and diagonal areas.

assimilated to stripes in the longitudinal view (purple box) and to circles perpendicular to the loading direction in the $r\theta$ plane (Figure 1d, scan A). The size of these "penny-shaped" cavities (especially their radial dimension, in the direction perpendicular to the loading axis) presents a large dispersion, but they all can be seen as flat cylinders in 3D. This kind of geometry has already been reported by Laiarinandrasana et al.[10] in the center of notched round bars deformed under steady strain rate up to the peak load and by Selles et al.[11] for similar specimens deformed under steady load up to the beginning of the tertiary creep stage.

Once the coalescence phenomenon is completed, voids are no longer flat cylindrical volumes of less dense matter and can be clearly characterized as penny-shaped and individual cavities. These cavities and their arrangements in the spherulitic microstructure are examined below.

**3.3. Voids Arrangement within the Spherulitic Microstructure.** *3.3.1. Different Regions of a Spherulite.* Figure 4 represents a diagram of a longitudinal view ($rz$ plane), related to a deformed spherulite encountered in semicrystalline polymers under tension (indifferently; polyamide, polypropylene, polyethylene, etc.). Initially, in the undeformed state, spherulites are similar to polygonal and multisided objects. However, they are generally idealized and defined as spheres. While the macroscopic engineering strain increases during the tensile test, spherulites are also subjected to tensile drawing. Thus, in longitudinal planes parallel to the loading direction (Figure 4), they can be represented with an elliptical contour. For the sake of clarity, several regions have been defined within these deformed spherulites. North and south poles denote extremities of the spherulite along the loading direction. Polar fan domains have been divided into north and south regions by
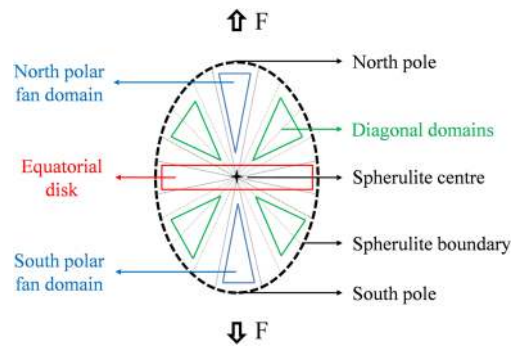
Laiarinandrasana et al.[19] in a study devoted to PP and PA6 materials. These areas can be represented by cones the bases of which are located at one pole and that converge toward the center of the spherulite. In a circumferential plane ($r\theta$ plane), perpendicular to the loading direction, spherulites have a circular shape. The circumferential plane that contains the center of the spherulite is denoted as the equatorial plane. The region represented in red in Figure 4 corresponds to the equatorial region of the spherulite and is denoted as the equatorial disk due to its circular boundary. The other areas, represented in green in Figure 4, are mainly constituted by lamellae rotated by about 45° with respect to the loading direction. These areas are denoted as the diagonal domains.

**3.3.2. Voiding State 2 mm Apart from the Neck (Scan B): Polar Fans or Equatorial Rings.** In scan B, two main mechanisms and cavities arrangements have been observed separately. Figure 5a displays, in 2D, by a longitudinal view (left) and in 3D (right) voids arranged in two conical columns parallel to the loading direction called polar fans.[15,16] Cavities are cylindrical and separated by walls of matter. The circular base of these voids is perpendicular to the loading direction and their diameters (length along the radial direction) are larger than their heights (lengths along the axial direction). The diameter of voids increases from the center of the spherulite to its north/south pole, forming two conical voided zones in the north and south polar fan domains (Figure 4). North and south voided fans[19] are not systematically observed simultaneously. In both scans A and B it is possible to observe voids showing only north or south fans, the other polar region of the spherulite remaining intact. Such an arrangement has also been observed
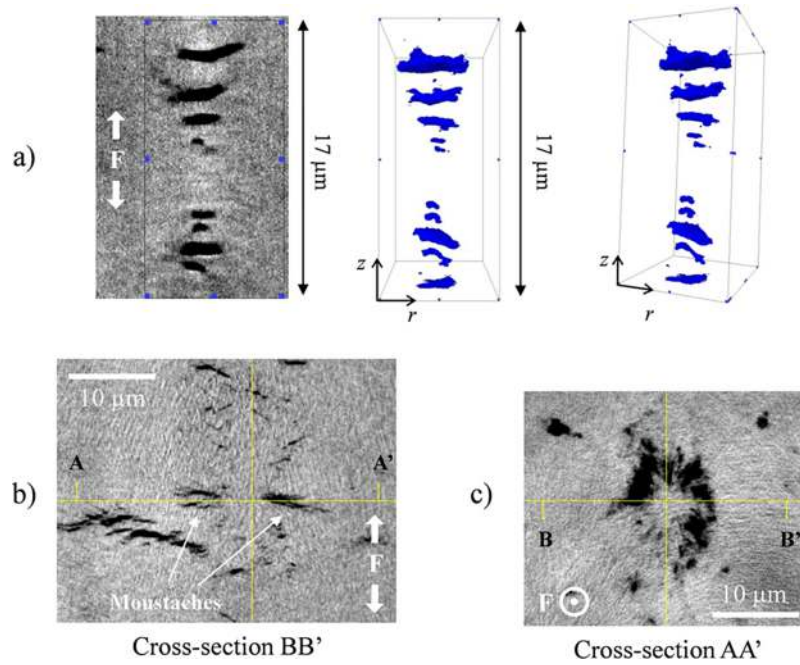
**Figure 5.** Scan B: (a) longitudinal (left) and 3D perspective views (right) of a polar fan; equatorial voiding observed (b) in the *rz* plane and (c) in the *rθ* plane.
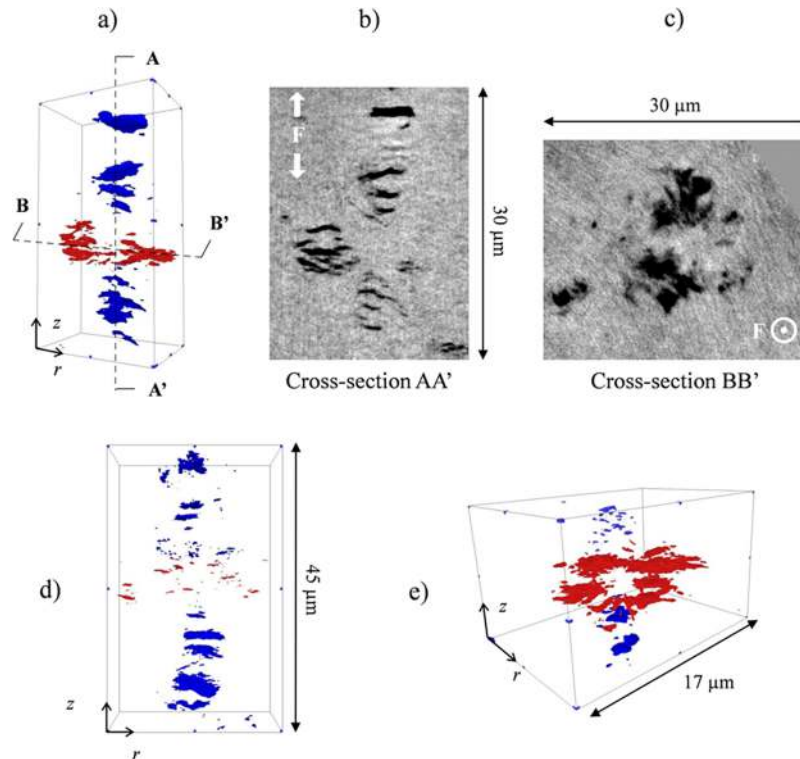


**Figure 6.** Scan A: (a) 3D view of multiple voided sites in the same spherulite; (b) corresponding longitudinal view of this arrangement; (c) corresponding circumferential view of this arrangement; (d) 3D view of voided polar fans (blue) with nascent equatorial voids; (e) 3D view of a voided equatorial ring (red) with nascent voids in the polar region.

by Laiarinandrasana et al.[10] in the extended neck of a smooth round bars made of the same PA6 material. The polar fan structure was the same but voids had undergone an extension along the loading direction, and their diameters were almost equal to their heights. This kind of voiding mechanism that takes place in the polar regions of spherulites has also been observed by Henning et al.[22] and Laiarinandrasana et al.[19] in PP. Between the north and south fans that form the two conical voided zones, an intact area (with no visible cavities) has been identified. This volume is located at the center of the spherulite and thus is called the unvoided center.

5

Table 2. Characteristic Lengths and Deformations of Polar Fans, Equatorial Rings, and Unvoided Centers: Mode Values

| | biggest cavity | | unvoided center | | voided zone | | intervoid |
|---|---|---|---|---|---|---|---|
| | $H_c$ | $D_c$ | $H_{uc}$ | $D_{uc}$ | $H_{pf}$ | $D_{er}$ | $H_{iv}$ |
| scan A | 0.6 | 4.5 | 8.5 | 3.75 | 21.5 | 16.5 | 2. |
| scan B | 0.6 | 3.0 | 6.75 | 4.25 | 17.5 | 8.5 | 1.4 |
| radial deformation $\varepsilon_r$ | | 0.5 | | −0.12 | | 0.94 | |
| axial deformation $\varepsilon_z$ | 0.0 | | 0.26 | | 0.23 | | 0.43 |
| volume variation $\Delta V/V_0$ | 1.0 | | 0.02 | | | | |
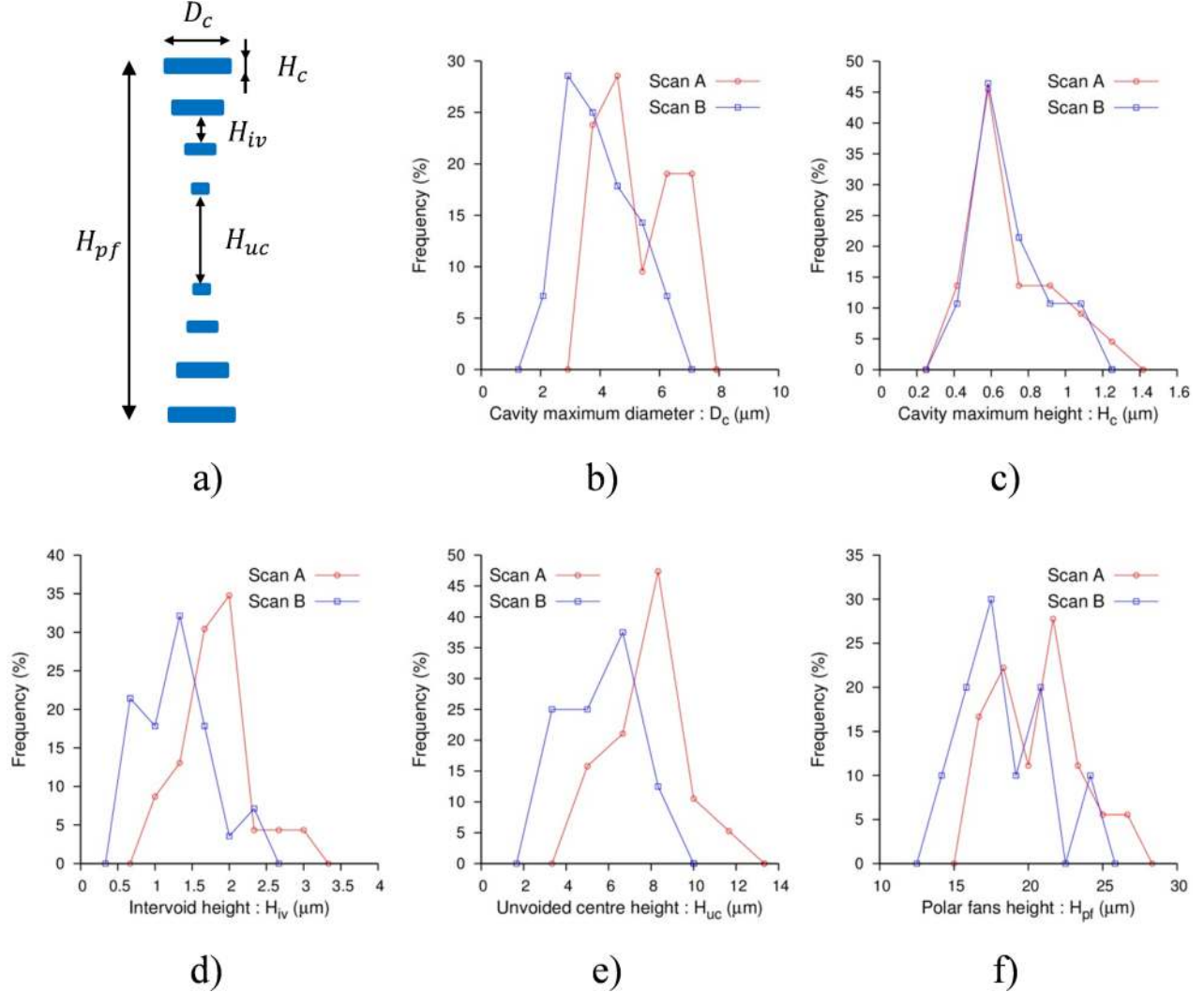


Figure 7. (a) Characteristic lengths of polar fans. Histograms for scans A and B of (b) cavity maximum diameter ($D_c$); (c) cavity maximum height ($H_c$); (d) intervoid height ($H_{iv}$); (e) unvoided center height ($H_{uc}$); (f) polar fans height ($H_{pf}$).

Another mechanism has been characterized in the circumferential plane (Figure 5c) by an unvoided circular center, surrounded by a diffuse and annular voided zone that converges toward this center. In the following, this kind of cavitation pattern will be denoted as equatorial rings because it occurs in the equatorial disk of the spherulites. In the $rz$ plane (Figure 5b), voids are arranged as moustaches on both sides of the intact center. Numerous authors have studied other semicrystalline polymers, PVDF[2] and PP[23] for instance, and have observed that cavitation took place in the equatorial amorphous phase of the spherulite, before yielding. They have also linked the whitening phenomenon in PP to confined groups of nanovoids in the equatorial disk of the spherulites.[24,25] Finally,

these equatorial rings are characterized by an unvoided and circular center surrounded by a diffuse and annular voided area in the $r\theta$ plane and by voids arranged in stripes on both sides of the unvoided center in the $rz$ plane.

*3.3.3. Voiding State in the Neck (Scan A): Multiple Voided Sites in the Same Spherulite.* Scan A has been centered on the revolution axis and located in the necking area, where the specimen diameter was the lowest and where $V_f$ was maximum. The voiding state was more advanced in scan A than in scan B where the two main cavitation mechanisms, polar fans and equatorial rings, have been observed separately. Figure 6a displays, in 3D, a combined configuration: polar fans (blue) and equatorial rings (red) have been observed simultaneously
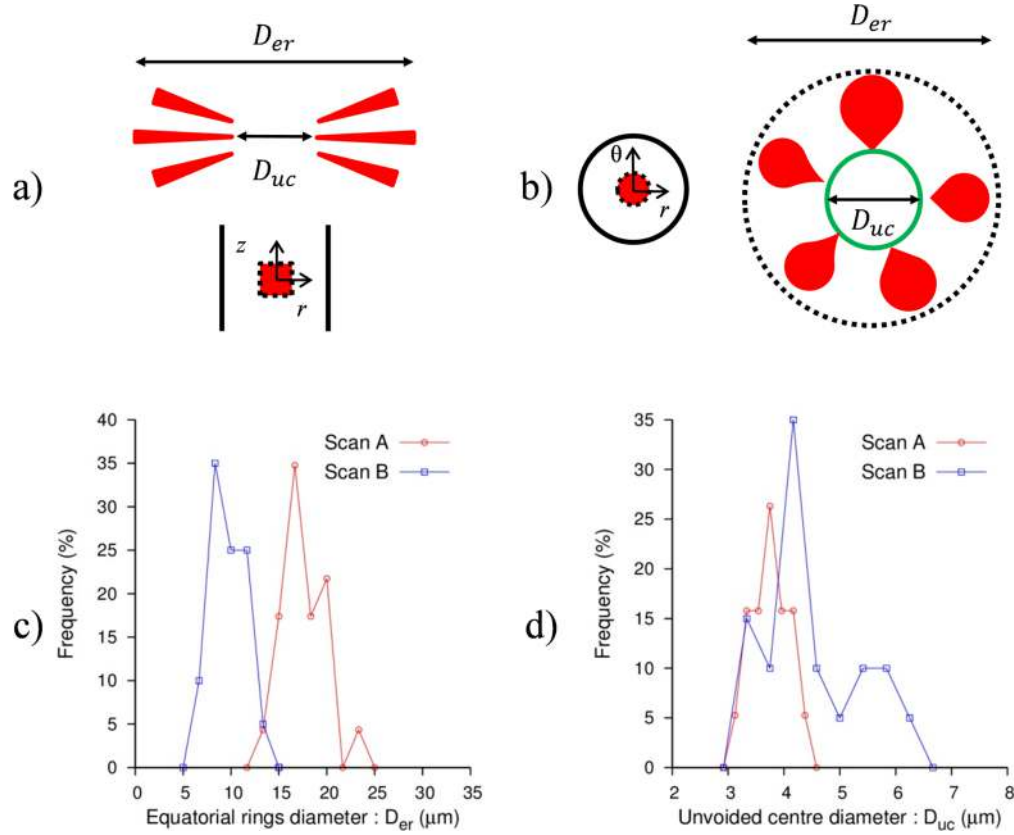
**Figure 8.** Characteristic lengths of equatorial rings. (a) Sketching in longitudinal view ($rz$ plane). (b) Sketching in circumferential view ($r\theta$ plane). Histograms for scans A and B of (c) equatorial rings diameter ($D_{er}$). (d) Unvoided center diameter ($D_{uc}$).

within the same spherulite. Figures 6b and 6c display respectively the corresponding longitudinal and circumferential 2D slices. However, no predefined scenario has been identified. Indeed, the three following scenarios have been observed: (i) polar fans and equatorial rings develop simultaneously (Figure 6a); (ii) polar fans develop first and then equatorial rings appears (Figure 6d); (iii) equatorial rings develop first and then polar fans appear (Figure 6e). This kind of combined voiding had already been observed by Galeski et al.[26] in deformed bulk PA6 using transmission electron microscopy. Cavities had been found in the equatorial disks of spherulites, between crystalline lamellae and in the polar parts between broken lamellae. Finally, cavitation took place in the region of the spherulite under tension, where lamellae were parallel to the tensile axis (polar regions) or perpendicular to the tensile axis (equatorial disks). In the zones subjected to compression or shear, typically diagonal and intermediate domains (Figure 4), lamellae are rotated at 45°, and cavitation has not been observed. For instance, Aboulfaraj et al.[27] have studied spherulitic structure of PP and have observed, by SEM, cavitation under tensile loading and no cavitation under shear loading. The same phenomenon has been noticed by G'sell et al.,[28] also in PP.

**3.4. Quantitative Study of Voiding Mechanisms.** Polar fans and equatorial rings as cavitation features in spherulites have been described qualitatively in the previous section. In this section, these specific voids arrangement will be studied quantitatively. In scans A and B (volumes of 110 $\mu$m$^3$) more than 20 voided spherulites have been identified thanks to the patterns presented in the previous sections. They have been studied individually by the characteristic lengths of polar fans, equatorial rings, and unvoided centers (described in the

following subsections). The results from scans A and B have been compared to highlight the evolution along the revolution axis of these characteristic lengths. Heights stand for dimensions along the loading direction and diameters for dimensions of circular patterns perpendicular to the loading direction. The mode value of the statistical data recorded for each characteristic dimension, corresponding to the value with the maximum frequency, has been chosen to depict the population of voids pattern and their dimensions in each scan. These results are summarized in Table 2. In scan C, the voiding state was not advanced enough, and the patterns of equatorial rings or polar fans have not been observed.

*3.4.1. Polar Fan Arrangement.* Figure 7a displays a complete schematic polar fan with north and south voided fans based on the observations of the real voids arrangement, presented in Figure 5a. $D_c$ and $H_c$ represent respectively the diameter and the height of the biggest individual and cylindrical cavity of the conical voided column. These cavities are located at the poles of the spherulites. In Figures 7b and 7c, respectively, histograms of $D_c$ and $H_c$ for the population of polar fans encountered in scans A and B have been superimposed. The histograms are centered on the mode value. For $D_c$, the mode value increases from 3.0 $\mu$m in scan B to 4.5 $\mu$m in scan A whereas the mode value of $H_c$ is 0.6 $\mu$m for both scans A and B. The height of polar fans biggest cavities remains constant along the revolution axis of the specimen and its diameter exhibit a gradient: $D_c$ is maximum within the neck (in scan A) and decreases when the position of the scan is shifted along the revolution axis (in scan B).

$H_{iv}$ stands for the height of the intervoids: the walls of matter that separate voids in polar fans. A single (north or south) fan is

7
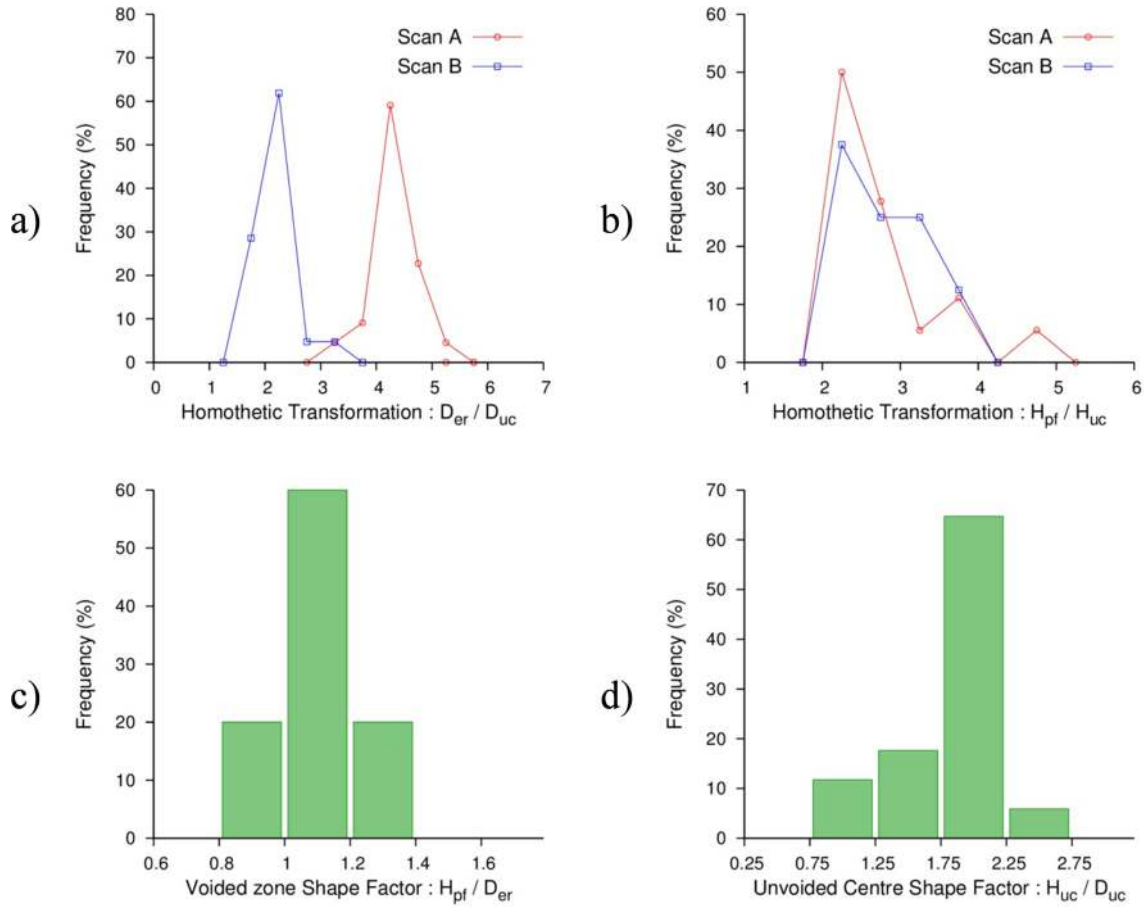
**Figure 9.** Histograms of (a) proportional relation $(D_{er}/D_{uc})$ and (b) proportional relation $(H_{pf}/H_{uc})$. (c) Voided zones shape factor $(H_{pf}/D_{er})$. (d) Unvoided centers shape factor $(H_{uc}/D_{uc})$.

constituted of 4 or 5 individual cavities, and $H_{iv}$ is defined as the mean value of intervoid heights in a single fan. Figure 7d displays histograms of $H_{iv}$ for scans A and B. The mode value is higher for polar fans located in scan A (2.0 $\mu$m) than for polar fans in scan B (1.4 $\mu$m).

$H_{uc}$ is the height of the unvoided center, i.e., the distance between the last cavities of the voided cones, at the summit of north and south fans. In Figure 7e histograms of unvoided centers height $(H_{uc})$ are plotted for polar fans located in scans A and B. The intact volumes at the center of the voided spherulites located in scan A are more extended in the loading direction (mode value of 8.5 $\mu$m for $H_{uc}$) than the intact volumes at the center of the voided spherulites in scan B (mode value of 6.75 $\mu$m for $H_{uc}$).

$H_{pf}$ represents the height of the complete polar fan, that is, the distance between the biggest cavity of the north fan and the biggest cavity of the south fan. The mode value of $H_{pf}$ increases from 17.5 $\mu$m in scan B to 21.5 $\mu$m in scan A (Figure 7f). The height of the voided zones in the polar and longitudinal region of the spherulites is maximal within the nascent neck.

*3.4.2. Equatorial Ring Arrangement.* Figures 8a and 8b display respectively schematic equatorial rings represented in longitudinal (moustaches like voids arrangement) and circumferential views (annular voided zones). These diagrams have been respectively based on the qualitative observations of cavities arrangement in the equatorial disks of the spherulites presented in Figures 5b and 5c. The equatorial voided zone represented in red, also called equatorial rings, and the

unvoided center, represented in green, present circular shapes in the circumferential view, and their diameters are respectively denoted $D_{er}$ and $D_{uc}$.

In Figures 8c and 8d, respectively, histograms of $D_{er}$ and $D_{uc}$ are compared for populations of spherulites voided in their equatorial disks within scans A and B. The mode value of $D_{er}$ is 16.5 $\mu$m for scan A and 8.5 $\mu$m for scan B. In scan B, the voided zone in the equatorial plane of the spherulites is less extended than in scan A. From scan B to A, porosity has progressed circumferentially in the equatorial part of the spherulite. Regarding the histogram of unvoided centers diameter (Figure 8d), the two distributions are centered on the mode value of 3.75 $\mu$m for scan A and 4.25 $\mu$m for scan B. The diameter of the intact volume at the center of the voided spherulites has slightly decreased from scans B to A.

*3.4.3. Homothetic Relationships.* Equatorial rings diameter $(D_{er})$ and unvoided centers diameter $(D_{uc})$ have been recorded for scans A and B. The ratio between these two diameters $(D_{er}/D_{uc})$ is reported for each voided spherulite, and a proportional relation between $D_{er}$ and $D_{uc}$ has been identified and described by the histograms in Figure 9a. Indeed, these distributions present sharply peaked modal values. 60% of the voided spherulites in scan A present a ratio $(D_{er}/D_{uc})$ of 4.25. 65% of the voided spherulites in scan B have a ratio $(D_{er}/D_{uc})$ of 2.25. At a given location, voids tend to have the same shape in the equatorial part of the spherulites: the diameter of the equatorial voided areas is 4.25 (respectively 2.25) times higher than the diameter of the unvoided volume at the center of these
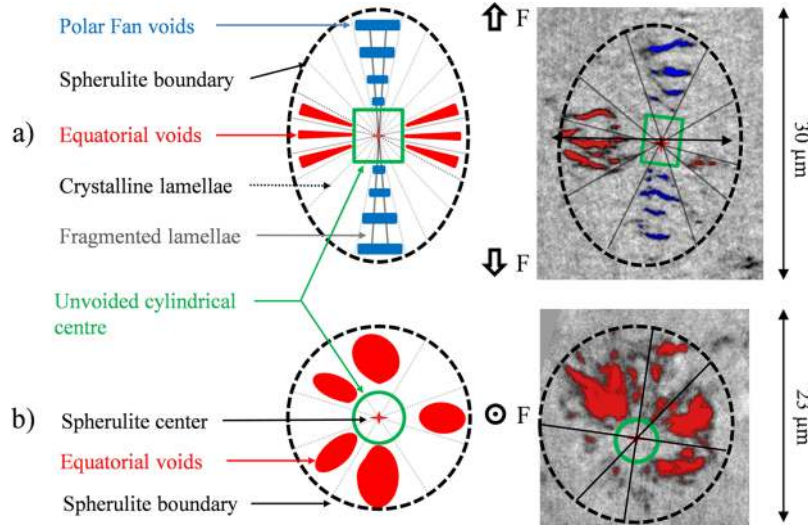
**Figure 10.** Diagrams of void arrangements within a deformed spherulite: (a) longitudinal view ($rz$ plane); (b) circumferential view ($r\theta$ plane).

spherulites in scan A (respectively in scan B). Finally, the factor of proportionality between $D_{er}$ and $D_{uc}$ (4.25 in scan A and 2.25 in scan B) can be considered as an indicator of the voiding state progress within the material, especially in the equatorial plane of the spherulites.

The longitudinal parts of the voided spherulites, along the $z$-axis, have been studied in Figure 7 for scans A and B. The proportional relation between $H_{pf}$ and $H_{uc}$ is highlighted for polar fans located in scans A and B by histograms of the ratio $H_{pf}/H_{uc}$ (Figure 9b). More than 50% of the voided spherulites present a ratio ($H_{pf}/H_{uc}$) of 2.25 in scan A. 40% of the voided spherulites have the same ratio ($H_{pf}/H_{uc}$) of 2.25 in scan B. The different domains (north and south voided fans domains and intact volume) are subjected to similar deformation along the loading axis from scan B to scan A, and the height of polar fans is 2.25 times higher than the height of the unvoided centers in spherulites observed in both scans A and B.

Finally, the frequencies of mode values for the ratios ($H_{pf}/H_{uc}$) and ($D_{er}/D_{uc}$) are higher than the ones obtained for the characteristic lengths considered individually in Figures 7 and 8. Studying these ratios reduces the impact of the experimental dispersion on spherulites initial sizes: the bigger the spherulite, the larger the intact center and the bigger the volume subjected to cavitation phenomena. Indeed, the diameter (respectively the height) of the voided zone is proportional to the diameter (respectively the height) of the unvoided center in a deformed spherulite.

*3.4.4. Shape Factors: In the Neck at the Peak Stress (Scan A).* As mentioned previously, mixed cavitation patterns (both polar fans and equatorial rings) have been observed in scan A (Figure 6a). Whereas, in scan B, spherulites have been identified as voided only in their equatorial plane or in their polar regions, and the mixed cavitation pattern has not been observed.

Figures 9c and 9d display respectively histograms of voided zones and unvoided centers shape factors defined as the ratio between their height and diameter (respectively $H_{pf}/D_{er}$ and $H_{uc}/D_{uc}$). 60% of the deformed spherulites are characterized by a voided zone with a shape factor of 1.1. Heights are larger than diameters, and voided zones are elongated along the loading direction. The same trend has been observed for unvoided centers: 65% of the intact volumes at the center of the voided

spherulites have a shape factor around 2 and are stretched along the loading direction. Working with shape factors has resulted in very high frequencies for the mode values and has reduced the impact of experimental dispersions.

## 4. DISCUSSION

**4.1. Local Deformations.** From the characteristic lengths of voided spherulites identified in scans A and B, local deformations of voids, voided zones (polar fans and equatorial rings), and intact volumes of matter (unvoided centers and intervoids) can be computed between these two different voiding states. Indeed, the voiding state in scan B can be considered as anterior as the voiding state in scan A. The results are given in Table 2.

The local radial deformation ($\varepsilon_r$) is computed from mode diameter evolution of the biggest cavities ($D_c$), unvoided centers ($D_{uc}$), and equatorial rings ($D_{er}$) that have circular shapes in circumferential planes. $\varepsilon_r$ is defined as the engineering strain from mode lengths in scan B to mode lengths in scan A: $\varepsilon_r = (D_A - D_B)/D_B$. $D_A$ and $D_B$ stand respectively for the mode diameter of the considered "object" (cavity, unvoided center or equatorial ring) in scans A and B. With this definition of the radial deformation, the mode lengths in scan B are considered as the gauge lengths. Radial deformations of the biggest cavities of the polar fans and of equatorial rings are respectively 0.5 and 0.94 and are positive: voids grown radially from scan B to scan A. On the other hand, unvoided centers have undergone a small shrinkage in diameter due to the uniaxial load applied. The radial deformation is negative and equal to −0.12. Locally, cavitation features can be related to volumetric deformation and are subjected to radial extension from scan B to scan A while the intact volumes at the center of the spherulites, and thus the safe matter, are subjected to radial contraction due to the macroscopic state of strain.

The local axial deformation ($\varepsilon_z$) is computed from mode heights evolution of biggest cavities ($H_c$), unvoided centers ($H_{uc}$), intervoids ($H_{iv}$), and polar fans ($H_{pf}$). Axial deformation is defined similarly to the radial deformation as an engineering strain from mode lengths in scan B to mode lengths in scan A, mode heights in scan B being the gauge lengths. $\varepsilon_z = (H_A - H_B)/H_B$. $H_A$ and $H_B$ stand respectively for the mode height of the considered "object" in scans A and B. Axial deformation of

the biggest cavities at the poles of the spherulites is zero. For the unvoided centers and the intervoids, the axial deformation is positive and of the same order (respectively 0.26 and 0.43). From scan B to scan A, the safe matter is subjected to local axial stretching. Finally, the axial deformation of the polar fans ($\varepsilon_z(H_{pf}) = 0.23$) is due to the axial deformations of its "components": unvoided center, intervoids, and cavities.

Both radial and axial deformations are known for the biggest cavities of the polar fans and for the unvoided volume at the center of the spherulites. The geometry of these objects being circular in the $r\theta$ plane, the problem can be considered as axisymmetric and $\varepsilon_\theta$ is assumed to be equal to $\varepsilon_r$. Finally, the volume change (defined as the trace of the strain tensor) can be calculated from

$$\frac{\Delta V}{V_0} = \varepsilon_z + 2\varepsilon_r$$

For the unvoided centers of the spherulites, the volume change between scan B and scan A is equal to 0.02 (Table 2), and these objects have almost endured an isochoric deformation. This quantitative result is in good accordance with the qualitative observations: there is a cylindrical volume at the center of the deformed spherulites with no visible voids up to the peak stress. For the biggest cavity of the polar fans, the volume change between scan B and scan A is positive and equal to 1.0 (Table 2). Individual and cylindrical voids produced by coalescence are then subjected to a volumetric growth phenomenon: up to the peak stress, the diameter increases while the height remains constant.

**4.2. Sketching of Voids Arrangement within the Spherulitic Microstructure: In the Neck at the Peak Stress (Scan A).** The two main mechanisms of voiding and their localization within the deformed spherulites have been presented in the previous sections. It has been highlighted that the voided zones progress radially in the equatorial plane of the spherulites from scan B to scan A and that both polar fans and equatorial rings could be found in the same voided spherulite. A theoretical illustration of these phenomena is proposed in Figure 10, and this representation has been compared with real cavitation patterns. In the longitudinal view (Figure 10a) the deformed spherulite has an elliptical shape, stretched longitudinally along the loading direction. The polar fan is represented in blue by flattened cylindrical cavities the circular bases of which are perpendicular to the loading direction. These individual cavities are organized in two conical columns called north and south polar fans that converge toward the center of the spherulite. The biggest cavities are located at the poles of the spherulite (see Figure 4). Moreover, the organization and the orientation of the crystalline lamellae within the spherulites play a major role in the micromechanisms of deformation and cavitation within semicrystalline polymers. In the north and south polar domains, lamellae are parallel to the loading direction and break under the tensile stress applied. Penny-shaped cavities then appear between the fragmented crystals. They are formed in the amorphous phase that has filled the empty space left between the fragments of lamellae.[15] The intact volume at the center of the spherulite has a rectangular shape in the longitudinal view, and on both its sides (in the equatorial part of the spherulite) the equatorial rings have been represented by red stripes that converge toward the center of the spherulite. In the equatorial disks of the spherulites, crystalline lamellae are oriented perpendicularly to the loading

direction and are separated by the tensile forces applied. Cavitation takes place, once again, in the interlamellar amorphous phase subjected to this tensile loading.[26,29] In the circumferential view (Figure 10b), the spherulite and its unvoided center have circular shapes. In 3D, the spherulite has a spheroidal shape elongated along the loading axis,[25] and the unvoided center can be considered as a cylinder with a circular base perpendicular to the loading direction. In the diagonal domains of the spherulites (Figure 4), subjected to shear loading, no voiding phenomena have been identified. Finally, in semicrystalline polymers, voids seem to develop within the spherulite, in an amorphous phase free to deform between broken or separated crystalline lamellae, subjected to tensile loading.

These observations could also be linked to the presence of an intact volume (with no visible voids) at the center of the spherulite. This cylindrical volume is deformed, stretched along the loading direction ($H_{uc}/D_{uc} = 2$ in scan A) but not voided. Voiding mechanisms taking place in the intraspherulitic amorphous phase; the authors suppose that the center of the spherulite is characterized by a higher local density of crystals and thus by a higher local crystallinity index than the other parts of the spherulite. The intralamellar amorphous phase at this location is not extensive and very constrained. This specific organization could be responsible for the quasi-isochoric deformation process of a volume (considered as initially spherical, as the whole spherulite itself) at the center of the spherulite with no visible cavitation.

Moreover, the size of the spherulites investigated also seems to play a key role in these cavitation mechanisms. Thomas et al.[30] have observed in a polybutene that large spherulites were subjected to intense cavitation and crazing whereas very little cavitation if any were observed within small spherulites. In scan A, the diameter of the voided zones is between 12 and 25 $\mu$m and their height between 15 and 28 $\mu$m. These lengths are much greater than the mean diameter of the spherical spherulite identified in the undeformed material (5 $\mu$m). Thus, voiding micromechanisms occurred preferably in big spherulites. The authors believe that little spherulites have an organization close to the one supposed in the unvoided center of the big spherulites, the density of crystals being high and the amorphous phase being not extensive enough and too much constrained to cavitate.

## 5. CONCLUSION

Smooth specimens in the form of round bars made of semicrystalline polyamide 6 (PA6) have been deformed under steady strain rate up to 50%, 75%, and 100% of the value of the engineering peak stress. The microstructure and the voiding state in these deformed samples have been observed in 3D at the European Synchrotron Radiation Facility (ESRF) with a resolution of 50 nm thanks to the magnified holotomography technique. This improved resolution has permitted the assessment of the early stages of cavitation in an unprecedented way.

In specimens submitted to monotonic tensile tests interrupted before the peak stress, only the population of pre-existing voids (spherical voids with a diameter between 0.1 and 0.5 $\mu$m) and very few clusters of nanometric voids have been observed. In the specimen deformed up to the peak stress, the coalescence phenomenon of a population of nanometric voids has been observed in the neck, leading to clusters of nanovoids and to cylindrical volumes of less dense matter than

the unvoided matrix. It finally results in the creation of individual and micrometric voids that can be assimilated to flat cylinders the circular basis of which are perpendicular to the loading direction.

The high resolution reached here has also allowed the study of the cavities arrangement within the spherulitic microstructure of the PA6. In the nascent neck, two main cavitation mechanisms have been observed simultaneously in a volume called scan A. Stacks of cylindrical voids, separated by walls of matter (intervoids), arranged in two conical columns parallel to the loading direction and separated by an unvoided cylindrical volume, have been observed and are called polar fans. Indeed, this phenomenon takes place in the polar regions of the spherulites. The other voiding process occurs in the equatorial disk of the spherulites and is called the equatorial ring: it consists in a diffuse and annular voided area that surrounds the intact volume located at the center of the spherulite. In a volume called scan B, shifted 2 mm away from the neck along the revolution axis of the specimen, the voiding state was less advanced, and the two mechanisms presented before have been observed separately. Finally, the diagonal domains of the spherulites (where the crystalline lamellae are rotated at about 45° with respect to the loading direction) are subjected to shear loading, and no voiding phenomena have been identified in these areas.

The characteristic dimensions of polar fan and equatorial ring arrangements have been evaluated in scans A and B. Voiding features (equatorial rings and biggest cavities of a polar fan) radial growth, seen from scans B to A, illustrates how the cavitation state progresses. The intact volumes of matter (unvoided cylindrical volumes at the center of the spherulite and intervoids in polar fans) are subjected to local axial stretching from scans B to A. Moreover, in both scans A and B, in a given deformed spherulite, the dimensions (diameter and height) of the voided zone are proportional to the dimensions of the intact volume at the center. They are correlated with the size of the spherulite and to the voiding state. In the neck (scan A), it is also possible to define shape factors (ratio between height and diameter) of the voided area (1.1) and of the unvoided volume at the center of the spherulite (2). These shape factors are greater than 1, and the objects inspected are stretched along the loading direction, according to the macroscopic deformation applied.

## AUTHOR INFORMATION

### Corresponding Author
*(N.S.) E-mail: nathan.selles@mines-paristech.fr.

### ORCID
Peter Cloetens: 0000-0002-4129-9091

### Notes
The authors declare no competing financial interest.

## REFERENCES
(1) Laiarinandrasana, L.; Morgeneyer, T.; Proudhon, H.; Regrain, C. Damage of semicrystalline polyamide 6 assessed by 3D X-ray tomography: From microstructural evolution to constitutive modeling. *J. Polym. Sci., Part B: Polym. Phys.* **2010**, *48*, 1516−1525.

(2) Castagnet, S.; Girault, S.; Gacougnolle, J.; Dang, P. Cavitation in strained pvdf: mechanical and x-rays experimental studies. *Polymer* **2000**, *41*, 7523−7530.

(3) Challier, M.; Besson, J.; Laiarinandrasana, L.; Piques, R. Damaged and fracture of polyvinylidene fluoride (PVDF) at 20°C: Experiments and modelling. *Eng. Fract. Mech.* **2006**, *73*, 79−90.

(4) Schirrer, R.; Fond, C.; Lobbrecht, A. Volume change and light scattering during mechanical damage in polymethylmethacrylate toughened with core-shell rubber particles. *J. Mater. Sci.* **1996**, *31*, 6409−6422.

(5) Rolland, H.; Saintier, N.; Robert, G. Damage mechanisms in short glass fibre reinforced thermoplastic during *in situ* microtomography tensile tests. *Composites, Part B* **2016**, *90*, 365−377.

(6) Boisot, G.; Laiarinandrasana, L.; Besson, J.; Fond, C.; Hochstetter, G. Experimental investigations and modeling of volume change induced by void growth in polyamide 11. *Int. J. Solids Struct.* **2011**, *48*, 2642−2654.

(7) Schirrer, R.; Lenke, R.; Boudouaz, J. Study of mechanical damage in rubber-toughened Poly(Methyl Methacrylate) by single and multiple scattering of light. *Polym. Eng. Sci.* **1997**, *37*, 1748−1760.

(8) Gehant, S.; Schirrer, R. Multiple light scattering and cavitation in two phase tough polymers. *J. Polym. Sci., Part B: Polym. Phys.* **1999**, *37*, 113−126.

(9) Humbert, S.; Lame, O.; Chenal, J. M.; Rochas, C.; Vigier, G. New insight on initiation of cavitation in semicrystalline polymers: in-situ SAXS measurements. *Macromolecules* **2010**, *43*, 7212−7221.

(10) Laiarinandrasana, L.; Morgeneyer, T.; Proudhon, H.; N'Guyen, F.; Maire, E. Effect of multiaxial stress state on morphology and spatial distribution of voids in deformed semicrystalline polymer assessed by X-ray tomography. *Macromolecules* **2012**, *45*, 4658−4668.

(11) Selles, N.; Nguyen, F.; Morgeneyer, T. F.; Proudhon, H.; Ludwig, W.; Laiarinandrasana, L. Comparison of voiding mechanisms in semi-crystalline Polyamide 6 during tensile and creep tests. *Polym. Test.* **2016**, *49*, 137−146.

(12) Selles, N.; Saintier, N.; Laiarinandrasana, L. Voiding mechanisms in semi-crystalline polyamide 6 during creep tests assessed by damage based constitutive relationships and finite elements calculations. *Int. J. Plast.* **2016**, *86*, 112−127.

(13) Cheng, Y.; Laiarinandrasana, L.; Helfen, L.; Proudhon, H.; Klinkova, O.; Baumbach, T.; Morgeneyer, T. F. 3D Damage Micromechanisms in Polyamide 6 Ahead of a Severe Notch Studied by In Situ Synchrotron Laminography. *Macromol. Chem. Phys.* **2016**, *217*, 701−715.

(14) Poulet, P. A.; Hochstetter, G.; King, A.; Proudhon, H.; Joannes, S.; Laiarinandrasana, L. Observations by in-situ X-ray synchrotron computed tomography of the microstructural evolution of semicrystalline Polyamide 11 during deformation. *Polym. Test.* **2016**, *56*, 245−260.

(15) Pawlak, A.; Galeski, A. Cavitation during tensile deformation of Polypropylene. *Macromolecules* **2008**, *41*, 2839−2851.

(16) Pawlak, A.; Galeski, A. Cavitation and morphological changes in polypropylene deformed at elevated temperatures. *J. Polym. Sci., Part B: Polym. Phys.* **2010**, *48*, 1271−1280.

(17) Morgeneyer, T. F.; Proudhon, H.; Cloetens, P.; Ludwig, W.; Roirand, Q.; Laiarinandrasana, L.; Maire, E. Nanovoid morphology and distribution in deformed HDPE studied by Magnified Synchrotron Radiation Holotomography. *Polymer* **2014**, *55*, 6439−6443.

(18) Regrain, C.; Laiarinandrasana, L.; Toillon, S.; Saï, K. Multimechanism models for semi-crystalline polymer: constitutive relations and finite element implementation. *Int. J. Plast.* **2009**, *25*, 1253−1279.

(19) Laiarinandrasana, L.; Selles, N.; Klinkova, O.; Morgeneyer, T. F.; Proudhon, H.; Helfen, L. Structural versus microstructural evolution of semi-crystalline polymers during necking under tension: Influence of the skin-core effects, the relative humidity and the strain rate. *Polym. Test.* **2016**, *55*, 297−309.

(20) Requena, G.; Cloetens, P.; Altendorfer, W.; Poletti, C.; Tolnai, D.; Warchomicka, F.; Degischer, H. P. Sub-micrometer synchrotron

tomography of multiphase metals using kirkpatrick-baez optics. *Scr. Mater.* **2009**, *61*, 760−763.

(21) Bleuet, P.; Cloetens, P.; Gergaud, P.; Mariolle, D.; Chevalier, N.; Tucoulou, R.; Susini, J.; Chabli, A. A hard x-ray nanoprobe for scanning and projection nanotomography. *Rev. Sci. Instrum.* **2009**, *80* (5), 056101.

(22) Henning, S.; Adhikari, R.; Michler, G. H.; Calleja, F. J. B.; Karger-Kocsis, J. Micromechanical Mechanisms for Toughness Enhancement in β-Modified Polypropylene. *Macromol. Symp.* **2004**, *214*, 157−172.

(23) Rozanski, A.; Galeski, A.; Debowska, M. Initiation of Cavitation of Polypropylene during Tensile Drawing. *Macromolecules* **2011**, *44*, 20−28.

(24) Farge, L.; André, S.; Pawlak, P.; Baravian, C.; Irvine, S.; Philippe, A. A study of the deformation induced whitening phenomenon for cavitating and non-cavitating semicrystalline polymers. *J. Polym. Sci., Part B: Polym. Phys.* **2013**, *51*, 826−841.

(25) Thomas, C.; Ferreiro, V.; Coulon, G.; Seguela, R. In situ AFM investigation of crazing in polybutene spherulites under tensile drawing. *Polymer* **2007**, *48*, 6041−6048.

(26) Galeski, A.; Argon, A. S.; Cohen, R. E. Changes in the morphology of bulk spherulitic nylon-6 due to plastic deformation. *Macromolecules* **1988**, *21*, 2761−2770.

(27) Aboulfaraj, M.; G'sell, C.; Ulrich, B.; Dahoun, A. In-situ observation of the plastic-deformation of polypropylene spherulites under uniaxial tension and simple shear in the scanning electron-microscope. *Polymer* **1995**, *36*, 731−742.

(28) G'Sell, C.; Dahoun, A.; Favier, V.; Hiver, J. M.; Philippe, M. J.; Canova, G. R. Microstructure transformation and stress-strain behavior of iso-tactic polypropylene under large plastic deformation. *Polym. Eng. Sci.* **1997**, *37*, 1702−1711.

(29) Keller, A.; Pope, D. P. Identification of structural processes in deformation of oriented polyethylene. *J. Mater. Sci.* **1971**, *6*, 453−478.

(30) Thomas, C.; Seguela, R.; Detrez, F.; Miri, V.; Vanmansart, C. Plastic deformation of spherulitic semi-crystalline polymers: An in situ AFM study of polybutene under tensile drawing. *Polymer* **2009**, *50*, 3714−3723.